

# Conducting Polymer Microcups for Organic Bioelectronics and Drug Delivery Applications

Martin Antensteiner, Milad Khorrami, Fatemeh Fallahianbijan, Ali Borhan, and Mohammad Reza Abidian\*

An ideal neural device enables long-term, sensitive, and selective communication with the nervous system. To accomplish this task, the material interface should mimic the biophysical and the biochemical properties of neural tissue. By contrast, microfabricated neural probes utilize hard metallic conductors, which hinder their long-term performance because these materials are not intrinsically similar to soft neural tissue. This study reports a method for the fabrication of monodisperse conducting polymer microcups. It is demonstrated that the physical surface properties of conducting polymer microcups can be precisely modulated to control electrical properties and drug-loading/release characteristics.

The development of sensitive and selective biosensors and bioelectronics is of considerable interest for neural interface technologies, including electrochemical biosensors and neural stimulation/recording probes.<sup>[1–5]</sup> The primary requirement of neural devices is to provide high density electrodes<sup>[6–11]</sup> that are biologically compatible with neural tissue, efficiently transduce biological signals to electronic signals, and remain functional for long periods of time. The performance of neural interfaces ultimately relies on the physical, chemical, and electrical properties of the electrode materials, which enable long-lasting functional communications. Existing electrodes utilize metallic materials that are often not intrinsically compatible with neural tissue, and cause reactive tissue responses and electrode encapsulation.<sup>[12–16]</sup> In addition, metallic electrodes suffer from poor electrical performance, including low signal-to-noise ratio and low charge-injection capacity, because of their planar microscale geometry. Several strategies have been reported to overcome these limitations and ultimately design a long-lasting functional interface. These strategies include optimizing the size, shape, and material of electrode

substrates,<sup>[12,17–19]</sup> coating electrodes with bioactive molecules,<sup>[20,21]</sup> electrodepositing conductive materials,<sup>[22–24]</sup> and delivering anti-inflammatory drugs.<sup>[25–29]</sup>

Conducting polymers (CPs) such as poly(pyrrole) (PPy) have gained considerable attention in neural applications<sup>[30–32]</sup> owing to 1) their soft mechanical properties that simulate those of biological structures; 2) their mixed electronic/ionic conductivity that promotes efficient signal transduction; 3) their transparency that allows the simultaneous use of optical analysis techniques; and 4) their facile functionalization with biomolecules

to tune biological responses.<sup>[31,33–35]</sup> CPs have been employed to improve the electrical performance of neural recording and stimulation, release drugs and proteins at the electrode–tissue interface, and enhance axonal regeneration.<sup>[24,36–40]</sup> Recent studies have produced a wide variety of CP micro and nanostructures, including nanoparticles,<sup>[41]</sup> microcavities,<sup>[42]</sup> microgrooves,<sup>[43]</sup> hollow microbottles,<sup>[44]</sup> microfibers,<sup>[45]</sup> nanofibers,<sup>[46]</sup> and microbowls.<sup>[47]</sup> Liu et al. chemically synthesized PPy poly(lactide-co-glycolide) (PLGA) nanoparticles to create PPy–PLGA core–shells.<sup>[41]</sup> Yang and Martin produced CP microcavities using polystyrene latex spheres as templates.<sup>[42]</sup> Hardy et al. fabricated aligned CP microgrooves using a patterned silk fibroin on polydimethylsiloxane templates.<sup>[43]</sup> Schmidt and co-workers fabricated CP nanofiber structures by combining electrospun PLGA nanofibers with chemical deposition of PPy to create PPy meshes in order to promote neurite outgrowth.<sup>[46]</sup> Qu et al. developed a method to construct multiple PPy microcontainers, including hollow microcups (MCs), microtubules, and microbowls.<sup>[44]</sup> They applied cyclic voltammetry (CV) to form bubbles on the stainless steel electrodes, which acted as templates for hollow microbottles, microfibers, and microbowls. Bajpai et al. used a similar approach with  $\beta$ -naphthalenesulfonic acid stabilized H<sub>2</sub> gas bubbles to fabricate CP microcontainers.<sup>[45]</sup> The CP microstructures enhance the electrical performance (i.e., decrease the impedance and increase the charge storage capacity) of microelectrodes by increasing the effective surface area.<sup>[47]</sup> Furthermore, during electrochemical polymerization, biomolecules can be incorporated within the CP microstructures as dopants in order to enhance the cellular interactions.<sup>[48,49]</sup> However, the incorporation of biomolecules may hinder the electrical properties of CPs, and the loading efficiency is limited by the doping level.<sup>[50]</sup> An additional challenge includes the creation of monodisperse

M. Antensteiner, M. Khorrami, Prof. M. R. Abidian  
Department of Biomedical Engineering  
University of Houston  
3517 Cullen Blvd, Room 2027, Houston, TX 77204, USA  
E-mail: mabidian@uh.edu

F. Fallahianbijan, Prof. A. Borhan  
Department of Chemical Engineering  
Pennsylvania State University  
University Park, PA 16802, USA

 The ORCID identification number(s) for the author(s) of this article can be found under <https://doi.org/10.1002/adma.201702576>.

DOI: 10.1002/adma.201702576

CP microstructures with tunable surface morphology including size, shape, and roughness.<sup>[2]</sup>

To overcome these challenges, we report a new templating method for the fabrication of monodisperse conducting polymer MCs with tunable surface morphology and electrical properties, controlled drug loading, and sustained drug release. The fabrication of CP MCs involves 1) electrospraying of monodisperse PLGA microspheres on gold (Au) substrates; 2) electrochemical polymerization of PPy around PLGA microspheres; and 3) dissolution of the PLGA microspheres. The surface morphology characteristics of PPy MCs, such as their height, opening diameter, and roughness, were precisely controlled by adjusting current density and electrodeposition time.

**Figure 1** shows a schematic of the fabrication process and optical images of PLGA microspheres and PPy MCs. PLGA microspheres were first electrosprayed on Au electrodes. PPy electrochemical polymerization was then initiated on the Au electrode, and subsequently advanced around the PLGA microspheres to form partially or fully coated PLGA microspheres (Figure 1c,e).<sup>[50–52]</sup> Finally, the PLGA microspheres were removed via dissolution from partially coated samples to form PPy MCs (Figure 1d). The effect of the electrospraying process parameters on the morphology and size of deposited PLGA particles was examined in an earlier study.<sup>[53]</sup> As shown in Figure 1f, the mean diameter of the electrosprayed PLGA microspheres in this study was  $3.22 \pm 0.23 \mu\text{m}$  with a coefficient of variance (CoV) of 7%, indicating a roughly monodisperse size distribution.<sup>[54,55]</sup>

The morphology of PPy MCs was characterized using scanning electron microscopy (SEM). **Figure 2a–e** and **Figure 2j–n** show progressive growth of PPy around PLGA microspheres for different deposition charge densities. As shown in these figures, the PLGA microspheres were partially coated with PPy for deposition charge densities of 30–180  $\text{mC cm}^{-2}$  (Figure 2a–d and Figure 2j–m), and fully coated at deposition charge density 240  $\text{mC cm}^{-2}$  (Figure 2e,n). Due to the CoV of microsphere size, a few fully coated microspheres were observed at deposition charge density 180  $\text{mC cm}^{-2}$ . After dissolution of PLGA from the partially coated microspheres, the produced PPy MCs did not collapse (Figure 2f–i and Figure 2o–r), presumably due to the mechanical strength of PPy microstructures.<sup>[40]</sup>

Materials confocal microscopy was utilized to map the surface topology and thickness of PPy films. **Figure 3a,b** shows color maps of surface elevation for electrode surfaces modified by PPy MCs that were produced with charge densities of 180  $\text{mC cm}^{-2}$  (partially coated PPy) and 240  $\text{mC cm}^{-2}$  (fully coated PPy), respectively. The measured PPy film thicknesses were  $62 \pm 35$ ,  $240 \pm 48$ ,  $488 \pm 99$ ,  $791 \pm 63$ , and  $802 \pm 101 \text{ nm}$  for deposition charge densities of 30, 60, 120, 180, and 240  $\text{mC cm}^{-2}$ , respectively. All thickness changes were significant ( $p < 0.001$ ) as the deposition current density increased except for increasing from 180 to 240  $\text{mC cm}^{-2}$  (Figure 3c). The surface roughness ( $R_q$ ) of PPy was characterized using atomic force microscopy, as shown in Figure 3d–i. The surface roughness increased linearly with deposition charge density, with measured values of 2.38 nm (bare gold) to 7.93, 10.6, 12.9, 16.0, and 16.7 nm for deposition charge densities of 30, 60, 120, 180, and 240  $\text{mC cm}^{-2}$ , respectively (Figure 3j).

As shown in Figure 2f–h, the circular footprint of the PPy MCs (uncoated Au) suggests that the PLGA microspheres were flattened at the bottom upon landing on the Au substrate. The circular Au footprint area and the cup opening diameter ( $D_x$ ) of the PPy MCs were measured to determine their basal diameter ( $D_b = 1.48 \pm 0.18 \mu\text{m}$ ) and height above the Au substrate ( $h_x$ ). The opening diameters were  $1.48 \pm 0.18$ ,  $1.82 \pm 0.15$ ,  $2.04 \pm 0.38$ ,  $2.11 \pm 0.24$ , and  $1.43 \pm 0.3 \mu\text{m}$  for deposition charge densities of 0, 30, 60, 120, and 180  $\text{mC cm}^{-2}$ , respectively. The opening diameter was 0  $\mu\text{m}$  for a deposition charge density of 240  $\text{mC cm}^{-2}$  because the PLGA microspheres were completely encapsulated by PPy in that case. Assuming a spherical cap shape for the PPy MCs, the MC height was calculated from

$$h_x = \frac{1}{2} D (\cos \beta_0 - \cos \beta) \quad (1)$$

where  $D$  is the mean diameter of PLGA microspheres and the spherical cap angle  $\beta_0$  and MC angle  $\beta$  (defined in **Figure 4a**) are related to  $D_b$  and  $D_x$  measurements according to

$$\beta_0 = \sin^{-1} \left( \frac{D_b}{D} \right) \quad (2)$$

and

$$D_x = D \sin \beta \quad (3)$$

The calculated MC heights were  $0.10 \pm 0.06$ ,  $0.18 \pm 0.15$ ,  $2.65 \pm 0.10$ ,  $2.88 \pm 0.15$ , and  $3.05 \pm 0.0 \mu\text{m}$  for deposition charge densities of 30, 60, 120, 180, and 240  $\text{mC cm}^{-2}$ , respectively (Figure 4c). There was a statistically significant difference ( $p < 0.001$ ) among all MC heights.

Based on a spherical cap shape for the PPy MCs, the measured opening diameter of each PPy MC was associated with a MC angle ( $\beta$ ) using Equation (3) represented by the dashed line in Figure 4b. The deposition charge density ( $\rho$ ) corresponding to each opening diameter measurement was thus associated with the MC angle for that measurement. In order to provide insight into the variation of opening diameter with deposition charge density, the deposition charge density associated with each data point was mapped onto the MC angle ( $\beta$ ) using a logistic function of the form

$$\frac{\beta - \beta_0}{180 - \beta_0} = a \left[ 1 + e^{-(\rho - \rho_0)/b} \right]^{-n} \quad (4)$$

where  $\beta$  is in degrees,  $\rho$  is in  $\text{mC cm}^{-2}$ , and  $\beta_0$  is the angle characterizing the diameter of the circular Au footprint of the PPy MC, as defined by Equation (2). The resulting mapping was used in conjunction with Equation (3) to establish the dependence of the opening diameter on deposition charge density, as shown by the dashed line in Figure 4c. The dashed line in this figure corresponds to values of  $a = n = 0.87$ ,  $b = 18$ , and  $\rho_0 = 97$  in Equation (4). As shown in Figure 4b,c, the mean opening diameter increased from  $1.48 \pm 0.18$  to  $2.04 \pm 0.38 \mu\text{m}$  as the deposition charge density increased from 0 to 60  $\text{mC cm}^{-2}$  and PPy growth on the PLGA microsphere advanced on the lower hemisphere ( $\beta < 90^\circ$ ). By contrast, the mean opening diameter

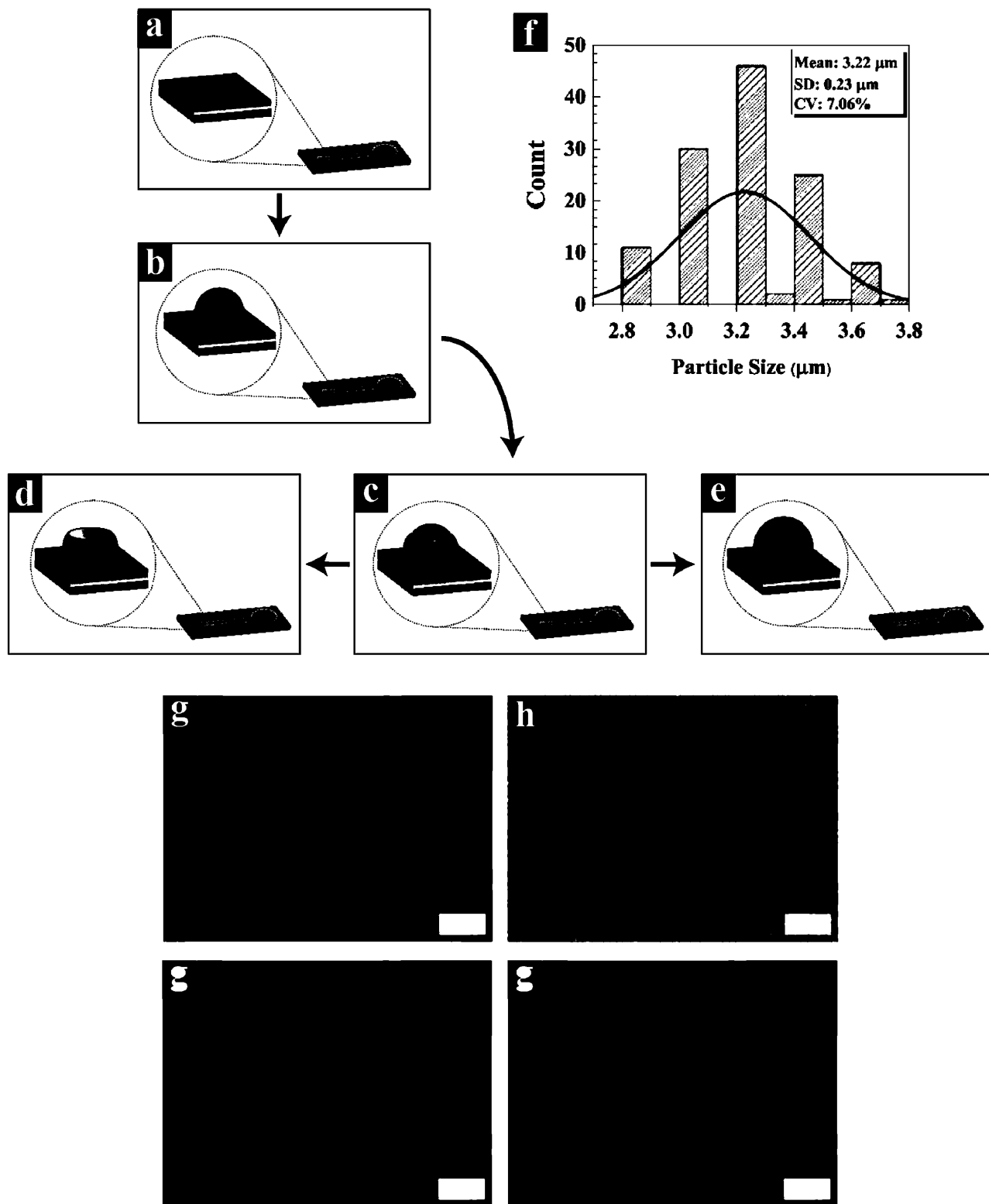


**Figure 1.** Schematic illustration of the PPy MC fabrication process including bright and dark field optical micrographs. a,g) Au electrodes before surface modification. b,h) Electrospayed PLGA microspheres on Au electrodes. c) Partial PPy encapsulation of PLGA microspheres. d,i) PPy MCs formed by dissolving PLGA microspheres. e,j) Full PPy encapsulation of PLGA microspheres. f) Histogram of PLGA diameter distribution. Scale bars = 20 μm.

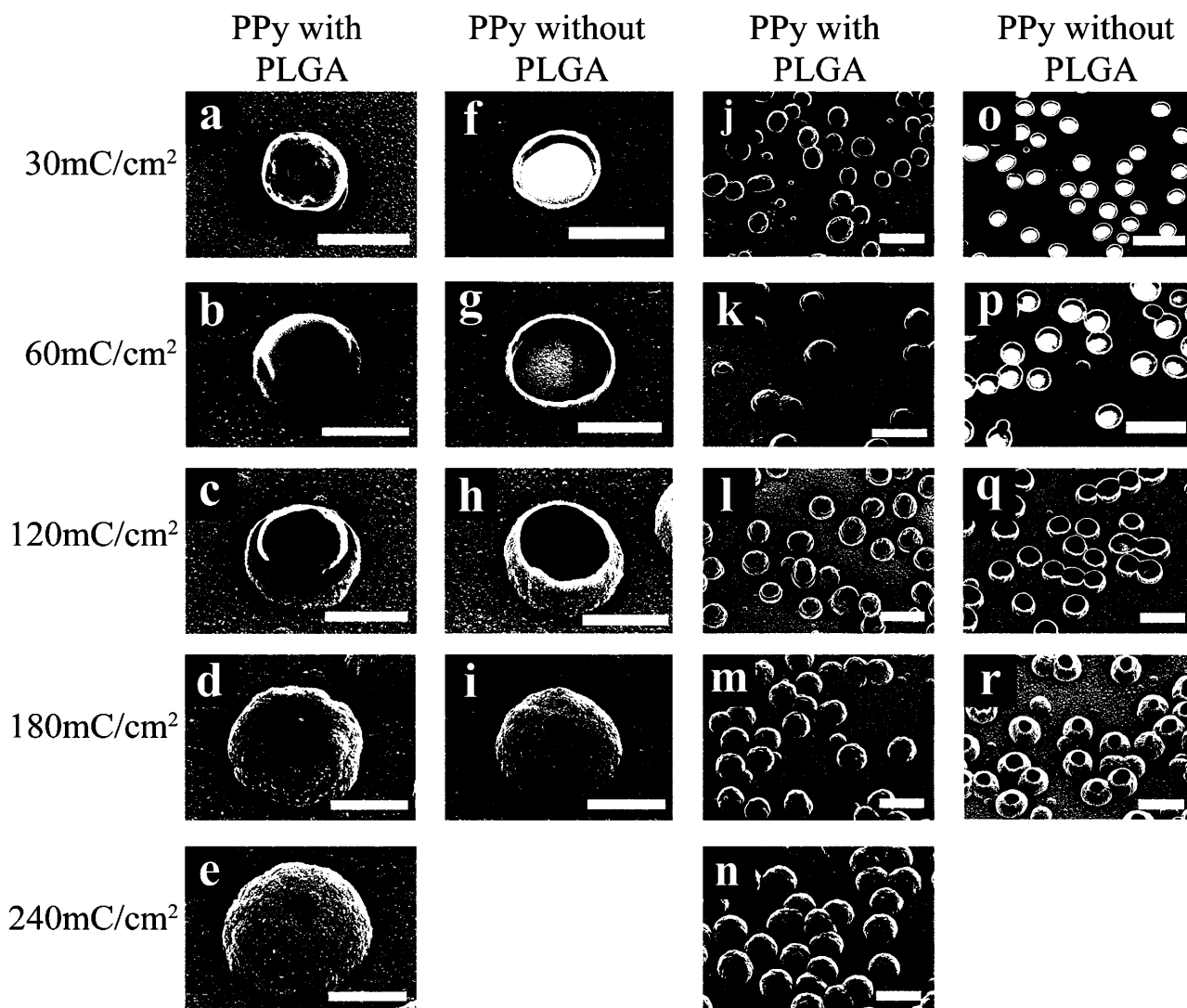


**Figure 2.** Scanning electron microscopy images of single a–e) and multiple j–n) PLGA microspheres partially coated with PPy at 30, 60, 120, and 180  $\text{mC cm}^{-2}$ , and fully coated at 240  $\text{mC cm}^{-2}$  deposition charge density (deposition current density of 0.5  $\text{mA cm}^{-2}$  and deposition time of 1, 2, 4, 6, and 8 min, respectively). f–i) single and o–r) multiple hollow PPy MCs following PLGA degradation. Scale bars = 2  $\mu\text{m}$  for (a)–(i) and 5  $\mu\text{m}$  (j)–(r).

decreased from  $2.11 \pm 0.11$  to  $1.47 \pm 0.3$   $\mu\text{m}$  as the deposition charge density was increased from 120 to 180  $\text{mC cm}^{-2}$ , due to PPy growth advancing on the upper hemisphere ( $\beta > 90^\circ$ ) for this range of deposition charge densities. According to the dashed line in Figure 4c, the maximum opening diameter was 3.23  $\mu\text{m}$ , which was achieved at a deposition charge density of 92  $\text{mC cm}^{-2}$ . For deposition charge densities less than 180  $\text{mC cm}^{-2}$ , the opening diameters were symmetrically distributed around the maximum opening diameter. For example, the opening diameters for deposition charge densities of 60 and 120  $\text{mC cm}^{-2}$  were the same because they were characterized by MC angles symmetric about the equator of PLGA microspheres (i.e., with the same values of  $|\beta - 90|$ ) as PPy growth crossed the equator. All opening diameters smaller (or larger) than the maximum diameter were statistically different ( $p < 0.001$ ).

The dependence of the height of PPy MCs ( $h_x$ ) on deposition charge density is shown by the solid line in Figure 4c. The predicted dependence was calculated by using Equation (4) for

the relation between deposition charge density and MC angle  $\beta$  in conjunction with Equations (1) and (2). The MC height was a monotonically increasing function of deposition charge density, increasing dramatically between 60 and 120  $\text{mC cm}^{-2}$  as the PPy coating advanced across the equator of the PLGA microsphere during this time. The MC height eventually reached a maximum of 3.05  $\mu\text{m}$ , as reflected by its value for deposition charge density of 240  $\text{mC cm}^{-2}$  when the PLGA microspheres were completely encapsulated by PPy. The maximum MC height was slightly smaller than the mean diameter of PLGA microspheres ( $3.23 \pm 0.23$   $\mu\text{m}$ ) because the microspheres were flattened at the bottom upon landing on the Au substrate. The surface area of PPy MCs was calculated according to Equations S5 and S6 (see the Supporting Information). The surface areas of the PPy MCs were  $0.23 \pm 0.09$ ,  $0.45 \pm 0.18$ ,  $6.1 \pm 0.24$ , and  $6.62 \pm 0.24$   $\text{mm}^2$  for deposition charge densities 30, 60, 120, and 180  $\text{mC cm}^{-2}$ , respectively. There was a statistically significant difference ( $p < 0.001$ ) among all surface area of PPy MCs.

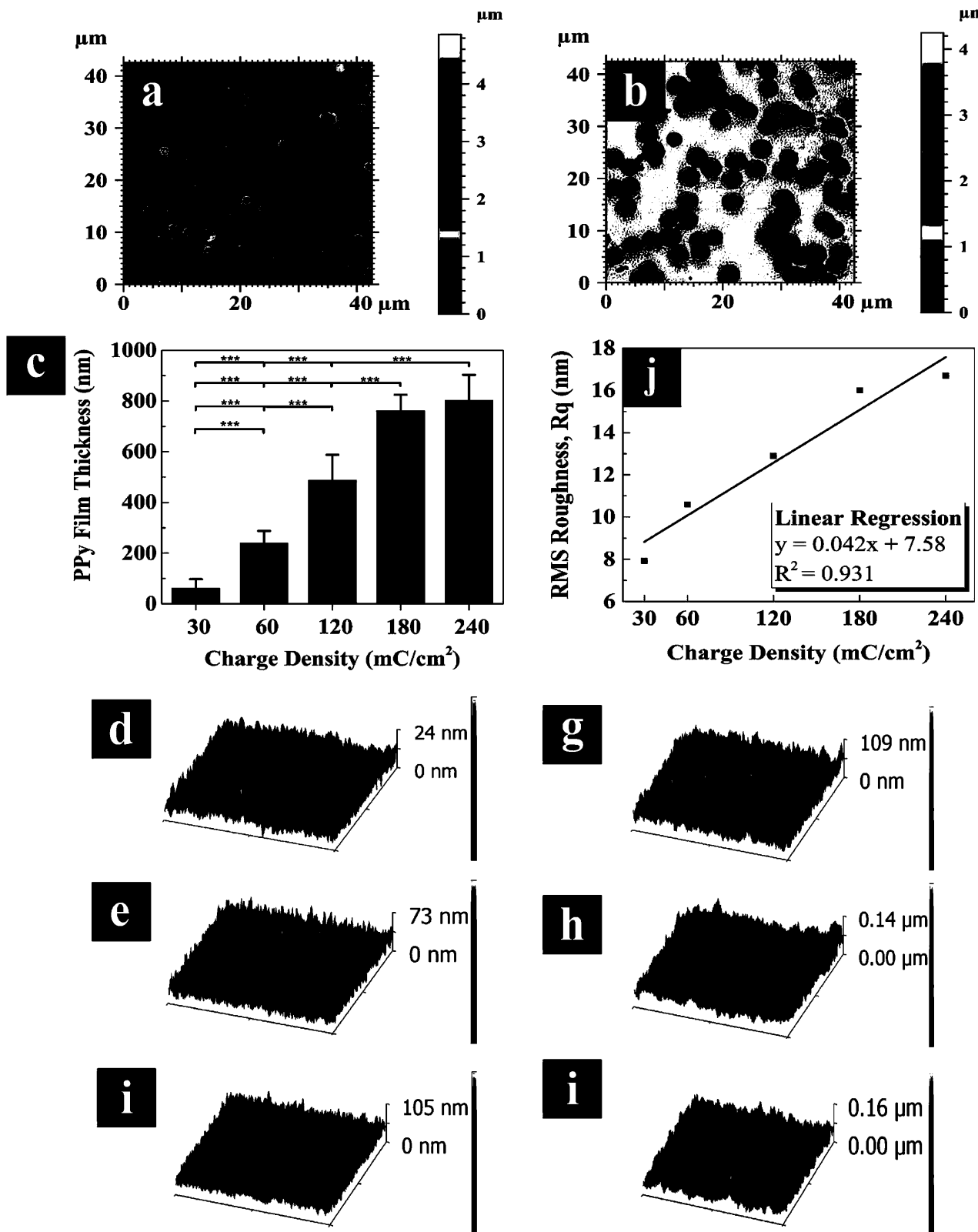


**Figure 3.** Thickness and roughness of PPy MCs. a,b) Color height maps of PPy MCs electrodeposited at  $180 \text{ mC cm}^{-2}$  to form partially coated microcups and at  $240 \text{ mC cm}^{-2}$  to form fully coated microcups, respectively. c) Bar graph of PPy film thickness as a function of applied charge density. The symbol \*\*\* indicates a significant difference of  $p < 0.001$ . d–i) Atomic force micrographs comparing the root-mean-square (RMS) roughness (Rq) of the bare gold surface and PPy films produced at 30, 60, 120, 180  $\text{mC cm}^{-2}$ , respectively. j) RMS roughness as function of applied charge density showing the linear increase in Rq as deposition charge density increased. Data are shown with a  $\pm$  SD ( $n = 5$ ).

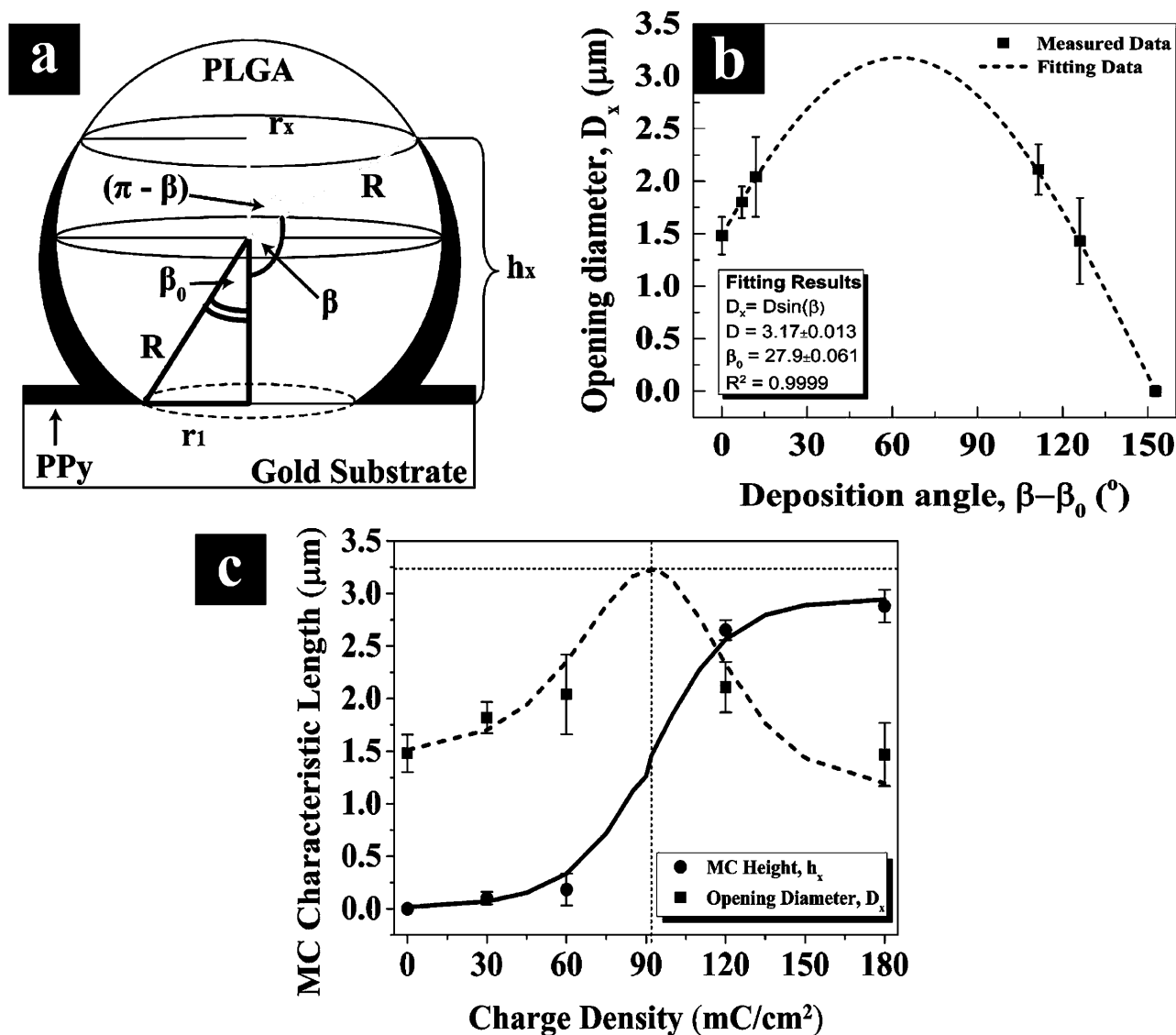


**Figure 4.** a) Schematic demonstrating the growth of PPy on PLGA microspheres at different deposition charge densities, which were used to calculate the MC characteristic lengths. Briefly, the area of both the Au circles and at the top opening of the PPy MCs were used to determine the opening diameter ( $D_x$ ), coating height ( $h_x$ ), the spherical cap angle  $\beta_0$ , and MC angle  $\beta$ . b) Plot showing fitted data of opening diameter mapped onto the MC angle using Equation (3). c) Plot showing the variation of opening diameter (blue squares) and MC height (red circles) with deposition charge density. To predict the dependence of the MC characteristic lengths on deposition charge density, each data set was fitted with a generalized logistic function in conjunction with Equations (1) and (2). For example, the maximum opening diameter ( $3.23 \mu\text{m}$ ) can be achieved at  $92 \text{ mC cm}^{-2}$  (dashed crosshair). Data are shown with a  $\pm$  SD ( $n = 50$ ).

Electrochemical impedance spectroscopy was used to investigate the electrical conductivity as the conducting polymer formed at different deposition charge densities. The formations of both PPy film and PPy MCs (i.e., PPy film/MCs) on Au electrodes contribute to their measured impedance. As shown in in **Figure 5a**, the impedance of Au electrodes was significantly reduced by the addition of PPy film/MCs. To examine the effect of PPy MCs on the impedance, PPy films were electrodeposited on gold electrodes (without PPy MCs) and the measured impedances of the PPy film electrodes were compared with those of their PPy film/MCs counterparts. As shown in **Figure 5c** for a frequency of 110 Hz, the PPy film electrodes (controls) had

lower impedances than their PPy film/MCs counterparts. That is because PPy film completely covered the surface of Au electrodes in the control experiments, whereas in the case of PLGA templates, uncoated gold remained exposed at the footprints of the MCs in the PPy film/MCs electrodes. There was no significant change in the impedance of the PPy film (control) electrode with increasing deposition current density, whereas the impedance of the PPy film/MCs electrode was significantly reduced ( $p < 0.001$ ) from  $714 \pm 42$  to  $624 \pm 47$ ,  $551 \pm 43$ , and  $506 \pm 59 \Omega$  as the deposition charge density increased from 30 to 60, 120, and  $180 \text{ mC cm}^{-2}$ , respectively. This can be explained by the significant increase in the PPy film/MCs

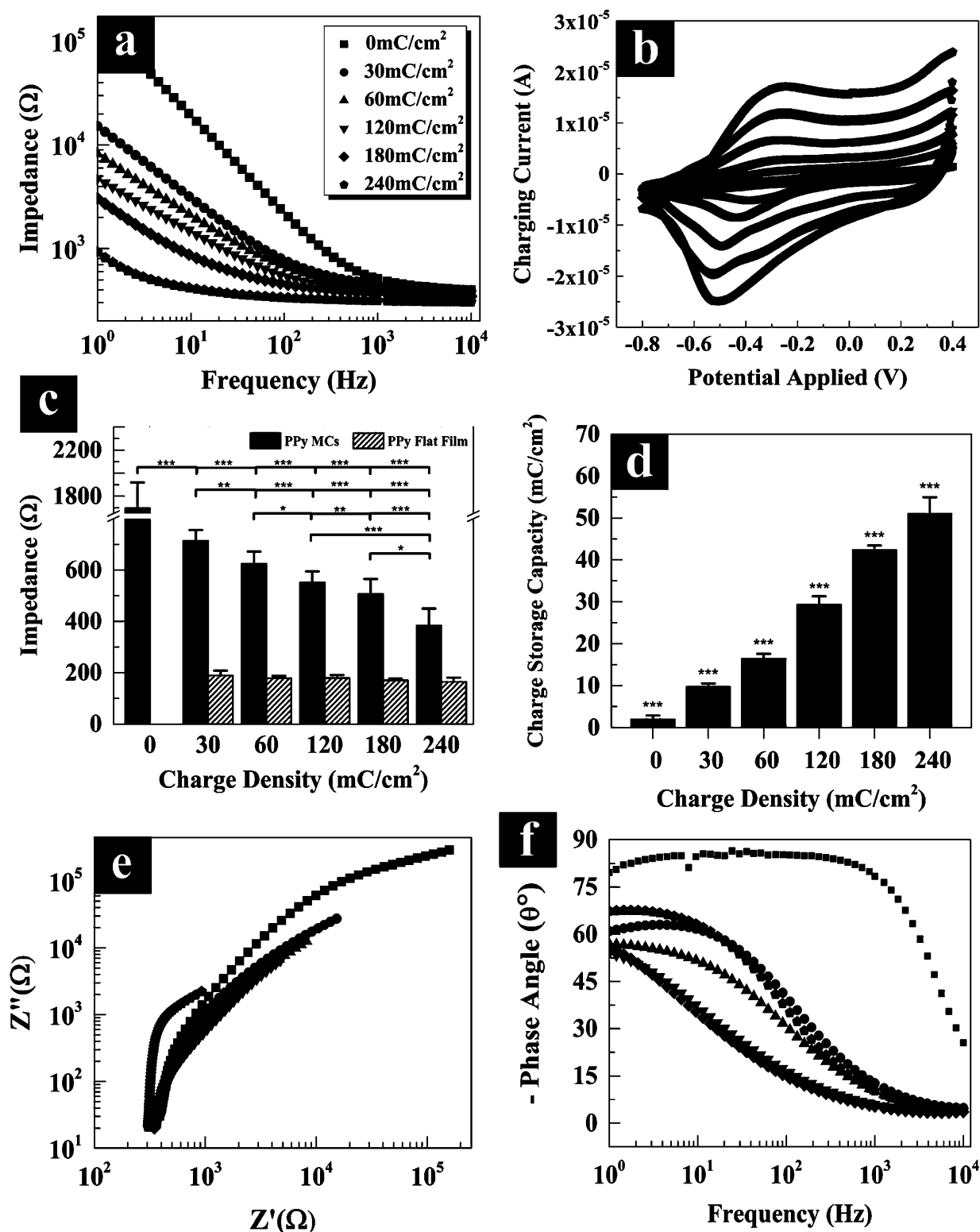


**Figure 5.** Electrical properties of Au electrodes modified with PPy MCs: bare gold (0 mC cm<sup>-2</sup>, black squares), 30 mC cm<sup>-2</sup> (red circles), 60 mC cm<sup>-2</sup> (blue triangles), 120 mC cm<sup>-2</sup> (magenta upside-down triangles), 180 mC cm<sup>-2</sup> (green diamonds), 240 mC cm<sup>-2</sup> (violet pentagon). a) Impedance spectrum over a frequency range of 1–10<sup>4</sup> Hz. b) Cyclic voltammetry, the potential swept from –0.8 to 0.4 V with a scan rate 30 mV s<sup>-1</sup>. c) Impedance at 110 Hz as a function of deposition charge density for PPy film/MCs (solid back) and PPy film without MCs (hatched gray). d) Charge storage capacity as a function of deposition charge density. e) Nyquist plot of impedance spectrum. f) Phase angle of impedance spectrum. Data are shown as  $\pm$  SD ( $n = 6$ ). The symbols \*\*\*, \*\*, and \* demonstrate significant difference  $p < 0.001$ ,  $p < 0.01$ ,  $p < 0.05$  between the groups, respectively.

surface area from  $1.82 \pm 0.09$  to  $2.04 \pm 0.18$ ,  $7.69 \pm 0.24$ , and  $8.21 \pm 0.24$  mm<sup>2</sup>, respectively, arising from the growth of MCs as the deposition charge density increased from 30 to 60, 120, and 180 mC cm<sup>-2</sup>. The minimum impedance of  $384 \pm 66$  Ω was achieved for a deposition charge density of 240 mC cm<sup>-2</sup>, showing that the completely closed PPy MCs resulted in ≈77% reduction in impedance compared to impedance of bare gold electrode ( $1696 \pm 223$  Ω, Figure 5c).

The Nyquist and phase angle plots in Figure 5e,f demonstrate the resistance and capacitance properties of electrodes. PPy film/MCs electrodes demonstrated a monotonic decrease in capacitive property with increasing frequency, with the highest reduction rate in capacitance occurring at lower frequencies as the deposition charge density increased from 30 to 180 mC cm<sup>-2</sup> (Figure 5e,f). The existence of PLGA microspheres inside of closed PPy MCs might be the reason for the different behavior observed for deposition charge density of 240 mC cm<sup>-2</sup>.

CV was performed to study the charge storage capacity of the PPy film/MCs formed at different deposition charge densities. The applied potential was swept between -0.8 and 0.4 V at a scan rate of 30 mV s<sup>-1</sup>. The surface area under the CV curve is proportional to the charge storage capacity.<sup>[50]</sup> As shown in Figure 5b, the charge storage capacity increased as deposition charge density increased. The charge storage capacities were  $2.04 \pm 0.78$ ,  $7.03 \pm 0.12$ ,  $13.5 \pm 0.37$ ,  $27.5 \pm 1.29$ ,  $40.5 \pm 1.19$ , and  $48.0 \pm 2.79$  mC cm<sup>-2</sup> for film/MCs formed at deposition charge densities 0, 30, 60, 120, 180, and 240 mC cm<sup>-2</sup>, respectively (Figure 5d). The increase in deposition charge density yielded a significant increase ( $p < 0.001$ ) in charge storage capacity among all groups. For example, at deposition charge density of 240 mC cm<sup>-2</sup>, an increase of ≈2300% was observed for charge storage capacity in comparison with the bare gold electrode (Figure 5d).

Figure 6 demonstrates the in vitro release profile of dexamethasone (DEX) from PPy film/MCs formed at different deposition charge densities. As described in the Experimental Section and depicted in Figures 6c–f, DEX was loaded on the surface of PPy film, outside and inside of PPy MCs. The DEX release was characterized by an initial burst release >65% in 2 h, followed by a sustained release of ≈10–15% over the next 250 h. The initial burst release is indicated by the intercept of the regression lines in Figure 6a. The deposition charge density had a significant effect on the initial burst release which increased from 66% at 30 mC cm<sup>-2</sup> to 78% at 180 mC cm<sup>-2</sup>. The increase in the initial burst release with increasing deposition charge density can be attributed to the larger surface area and roughness of the PPy at higher charge density, as shown by the positive correlation in Figure 6b. As shown in Figure 6a, the slow release after the first 2 h exhibited a square root of time dependence for all deposition charge densities. The observed time dependence of the sustained release is consistent with that predicted for diffusion of the drug out of a PPy that is initially impregnated with a uniform concentration of DEX.<sup>[53]</sup> The rate of sustained release was not significantly affected as the deposition charge density increased from 30 to 180 mC cm<sup>-2</sup>, indicating that drug release was dominated by diffusion out of the planar PPy on the 1.0 × 1.5 cm electrodes used for

drug release experiments. This is not surprising considering that the total surface area of PPy MCs changed from 0.23 to 6.62 mm<sup>2</sup> (representing less than 5% of the planar area of the electrode) as the deposition charge density increased from 30 to 180 mC cm<sup>-2</sup>. We demonstrated a novel method for the fabrication of conductive PPy MCs with tunable size, surface roughness, electrical properties, and drug release. We showed that an anti-inflammatory drug could be loaded within PPy microstructures and slowly released. The developed PPy MCs can be utilized for applications in the fields of bioelectronics and drug discovery.

## Experimental Section

**Materials:** PLGA (85:15 DLG 7E) with an inherent viscosity of 0.6–0.8 dL g<sup>-1</sup> was purchased from Evonik Industries (Birmingham, AL). Benzyltriethylammonium chloride (BTEAC) and pyrrole (Py,  $M_w$  67.09 g mol<sup>-1</sup>) were purchased from Sigma-Aldrich. Poly (sodium-p-styrenesulfonate) (PSS,  $M_w$  70 kD) was purchased from Acros-Organics. Chloroform was purchased from SupraSolv Company. N-type Si wafers coated with SiO<sub>2</sub> were purchased from University Wafer Company. Dexamethasone 21-phosphate disodium salt, 98% was purchased from Alfa Aesar.

**Fabrication of Conductive Substrates:** Au electrodes were fabricated on Si wafers (two circular areas with diameters 1.5 and 5.0 mm, connected with a 1 × 10 mm rectangular area) using electron beam evaporative deposition and laser-cut adhesive masks. A thin (10 nm) layer of titanium was deposited first to facilitate adhesion of the (100 nm) Au layer to the Si wafers.

**Fabrication of Electrospayed Microspheres:** Homogeneous solutions of 4% (w/w) PLGA and 2% BTEAC (w/w PLGA) were prepared by dissolving 617 mg of PLGA and 12.3 mg of BTEAC in 10 mL of chloroform at room temperature for 12 h. The mixture was electrospayed for 25 s using an applied field of 100 kV m<sup>-1</sup> (8 kV applied potential and 8 cm syringe–substrate separation distance), a spinneret gauge of 22, and a flow rate of 500 μL h<sup>-1</sup>. Temperature and humidity were controlled at 22 °C and 30–34%, respectively. The resulting PLGA microspheres deposited onto the 1.5-mm-diameter circular conductive substrate.

**Electrochemical Deposition of Conducting Polymers:** Electrochemical polymerization was performed using Autolab PGSTAT 302N (USA METROHM Company) in galvanostatic mode with a two-electrode configuration at room temperature. PLGA microspheres were coated with PPy using a solution containing 0.2 M Py and 0.2 M PSS as dopant, and applying a 0.5 mA cm<sup>-1</sup> current density over five different charge densities. The working electrode was applied to the substrates, while the counter electrode was connected to a platinum wire in the Py–PSS solution. After electrodeposition, the PLGA microspheres were dissolved in chloroform overnight to create PPy MCs.

**Electrochemical Impedance Spectroscopy (EIS):** EIS measurements were made by using an Autolab PGSTAT 302N and Nova Frequency Response Analyzer software in potentiostatic mode. A solution of 0.1 M phosphate-buffered saline (PBS, pH = 7.4) was used as the electrolyte in a three-electrode configuration. The Ag/AgCl reference electrode, Pt foil counter electrode, and fabricated electrodes were immersed in the PBS solution. A sinusoidal AC signal with 10 mV rms amplitude was imposed to measure the impedance magnitude over a frequency range of 1–10<sup>4</sup> Hz.

**CV:** A staircase CV was performed using an Autolab PGSTAT 302N in the three-electrode configuration. The potential on the working electrode was swept in the range of -0.8 to 0.4 V versus the reference electrode at a scan rate of 30 mV s<sup>-1</sup>. In order to calculate the charge storage capacity, the third cycle was used since the readings were observed to be consistently stable after the second cycle. The surface area contained inside the CV curve was determined using OriginLab software, and was used to calculate the charge storage capacity.

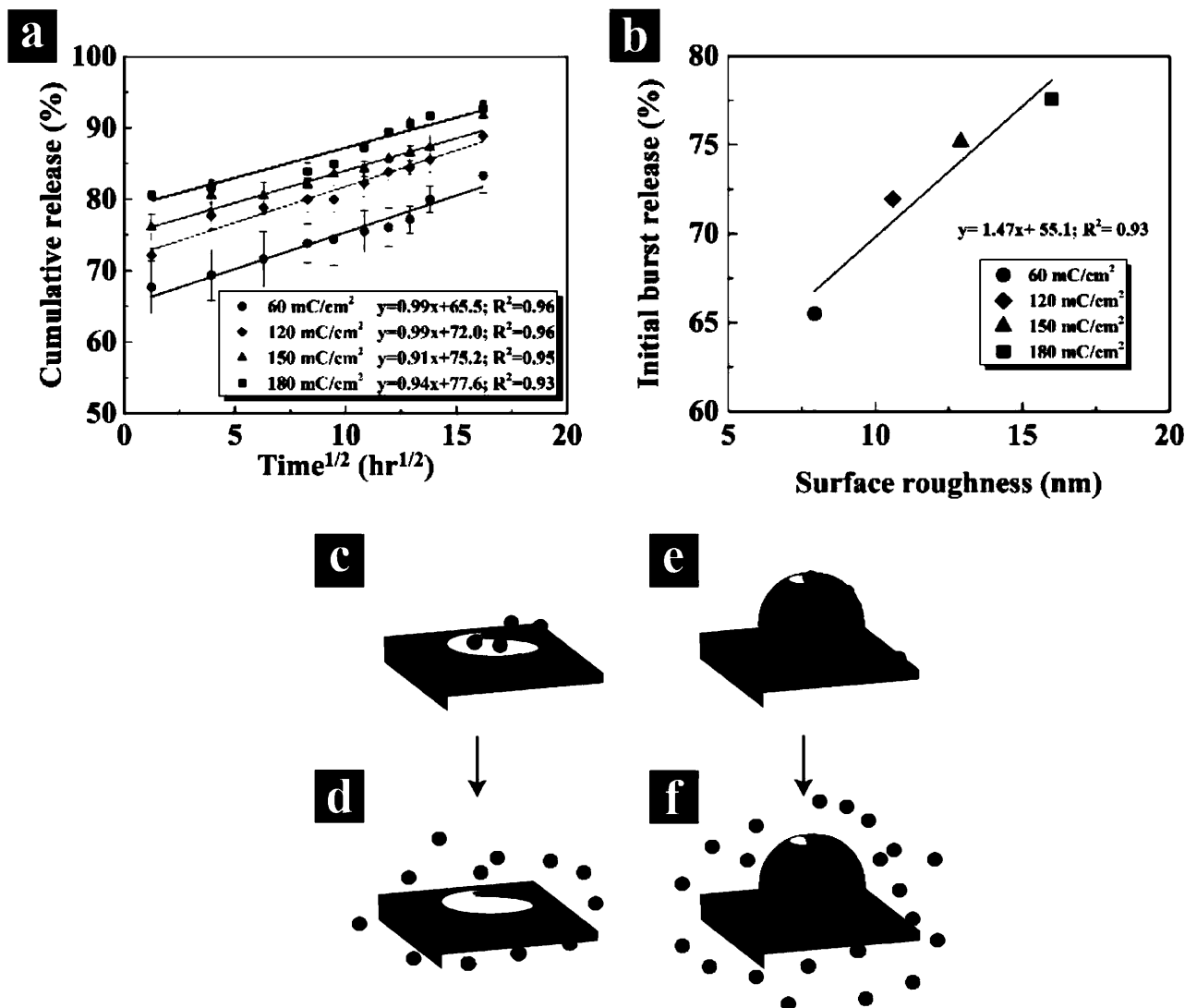


**Figure 6.** In vitro release study of DEX from PPy MCs: a) Plot showing the in vitro fitted release profile of DEX from PPy MCs as a function of deposition charge density  $60 \text{ mC cm}^{-2}$  (black squares),  $120 \text{ mC cm}^{-2}$  (orange diamonds),  $150 \text{ mC cm}^{-2}$  (blue triangles), and  $180 \text{ mC cm}^{-2}$  (red squares), data are shown with a  $\pm$  SD ( $n = 5$ ). b) Plot showing the correlation of initial burst release with surface roughness. Data points are charge densities of  $60 \text{ mC cm}^{-2}$  (black circle),  $120 \text{ mC cm}^{-2}$  (orange diamonds),  $150 \text{ mC cm}^{-2}$  (blue triangles), and  $180 \text{ mC cm}^{-2}$  (red squares). c–f) Schematic of DEX loading and release from PPy film/MCs with different MC heights and opening diameters.

**Morphology:** To characterize the size of the electrospayed PLGA microspheres, optical images were taken at  $50\times$  magnification (Zeiss Imager Z1, Germany) and analyzed using Axiovision digital processing software. After PPy coating, the conductive microstructures were mounted on aluminum stubs using carbon tape, and sputtered with gold (Denton Sputter Coater) for 40 s at 40 mA in order to reduce charging effect. The height, opening diameter, and surface morphology of PPy MCs were characterized using Field Emission Scanning Electron Microscope (FESEM, FEI Helios NanoLab 660). Image contrast and brightness were enhanced with Adobe Photoshop. The opening areas of PPy MCs were determined using Image J software, and subsequently used to calculate the dimensions of the PPy MCs. AFM in tapping mode using Si tips (force constant  $0.4 \text{ N m}^{-1}$ ) was performed on a  $25 \mu\text{m}^2$  area in the same central location on each electrode to determine the root-mean-square (Rq) surface roughness. PPy film thickness was determined using materials confocal microscopy (Zeiss Observer 1, Germany). The thickness of the Cr/Au electrodes on the Si wafers was first determined through a z-stack experiment and quantified using Confomap software

(Zeiss, Germany) to determine the step height according to ISO 5436 standards. After deposition at each deposition charge density, the same edge of each electrode was scanned again. The difference in step heights yielded the PPy film thickness ( $n = 5$  per deposition charge density).

**In Vitro Release Study:** The release of DEX was monitored as a function of incubation time in DI water at  $37^\circ\text{C}$ . The number of samples for each group was four ( $n = 5$ ). PPy MCs were fabricated on  $1 \times 1.5 \text{ cm}$  Au electrodes according to the previously described protocol of electrospaying and electrodeposition methods.<sup>[50–52]</sup> DEX ( $25 \text{ mg}$ ) was dissolved in  $1000 \text{ mL}$  of DI water to create solutions with a concentration of  $0.025 \text{ mg mL}^{-1}$ . All samples were sterilized with UV light for 24 h. In order to load the samples,  $1 \text{ mL}$  of DEX solution was pipetted onto each substrate, and degassed using low vacuum (Welch model 2026). Samples were kept in an incubator (Galaxy 170S, New Brunswick) at  $37^\circ\text{C}$  for 24 h. This process was performed three times. The samples were then immersed in  $4 \text{ mL}$  DI water. The concentration of released DEX was measured at specific times using UV–Vis spectrophotometry (Molecular Devices SpectraMax M5) at  $242 \text{ nm}$  wavelength.

*Statistical Analysis:* PLGA microspheres were analyzed by focusing on a predetermined central area of each optical image and measuring all microspheres within that area. Standard statistical analysis (Origin 8.6 SRO, Northampton, MA) was performed on these microspheres ( $n = 100\text{--}200$ ). PPy MC height and opening diameter were calculated as described, and processed in Origin ( $n = 50$  for each coating time). Outliers were removed by use of a Grubbs Test with a significance of 0.05 (standard two-sided analysis). ANOVA was performed on the results for MC opening diameter, MC height, PPy film roughness, impedance, and CV (OriginPro 2015).

## Supporting Information

Supporting Information is available from the Wiley Online Library or from the author.

## Acknowledgements

M.A. and M.K. contributed equally to this work. M.A., M.K., A.B. and M.R.A. designed the experiments, analyzed the data, and wrote the paper; M.A. and M.K. performed the research; F.F. contributed to partially record the impedance and CV; A.B. and M.R.A. directed the research. Funding was provided by the National Institutes of Health, National Institute of Neurological Disorders and Stroke grant number R01 NS087224. Special acknowledgment is made to Trevor Clark from the Materials Research Institute at Penn State University for his assistance with acquiring SEM images.

## Conflict of Interest

The authors declare no conflict of interest.

## Keywords

conducting polymers, drug release, microelectrodes, neural interfaces

Received: May 8, 2017

Revised: July 8, 2017

Published online:

- [1] T. Stieglitz, H. Beutel, M. Schuettler, J. U. Meyer, *Biomed. Microdevices* **2000**, *2*, 283.
- [2] P. Fattahi, G. Yang, G. Kim, M. R. Abidian, *Adv. Mater.* **2014**, *26*, 1846.
- [3] M. Gerard, A. Chaubey, B. D. Malhotra, *Biosens. Bioelectron.* **2002**, *17*, 345.
- [4] A. B. Schwartz, X. T. Cui, D. J. Weber, D. W. Moran, *Neuron* **2006**, *52*, 205.
- [5] D. R. Kipke, W. Shain, G. Buzsaki, E. Fetz, J. M. Henderson, J. F. Hetke, G. Schalk, *J. Neurosci.* **2008**, *28*, 11830.
- [6] J. C. Williams, R. L. Rennaker, D. R. Kipke, *Brain Res. Protoc.* **1999**, *4*, 303.
- [7] G. Buzsaki, *Nat. Neurosci.* **2004**, *7*, 446.
- [8] K. L. Drake, K. D. Wise, J. Farraye, D. J. Anderson, S. L. Bement, *IEEE Trans. Biomed. Eng.* **1988**, *35*, 719.
- [9] D. R. Kipke, R. J. Vetter, J. C. Williams, J. F. Hetke, *IEEE Trans. Neural Syst. Rehab. Eng.* **2003**, *11*, 151.
- [10] P. J. Rousche, R. A. Normann, *J. Neurosci. Methods* **1998**, *82*, 1.
- [11] D. H. Kim, J. Vimenti, J. J. Amsden, J. L. Xiao, L. Vigeland, Y. S. Kim, J. A. Blanco, B. Panilaitis, E. S. Frechette, D. Contreras, D. L. Kaplan, F. G. Omenetto, Y. G. Huang, K. C. Hwang, M. R. Zakin, B. Litt, J. A. Rogers, *Nat. Mater.* **2010**, *9*, 511.
- [12] V. S. Polikov, P. A. Tresco, W. M. Reichert, *J. Neurosci. Methods* **2005**, *148*, 1.
- [13] K. D. Wise, *IEEE Eng. Med. Biol. Mag.* **2005**, *24*, 22.
- [14] T. D. Y. Kozai, N. B. Langhals, P. R. Patel, X. P. Deng, H. N. Zhang, K. L. Smith, J. Lahann, N. A. Kotov, D. R. Kipke, *Nat. Mater.* **2012**, *11*, 1065.
- [15] T. D. Y. Kozai, K. Catt, X. Li, Z. V. Gugel, V. T. Olafsson, A. L. Vazquez, X. T. Cui, *Biomaterials* **2015**, *37*, 25.
- [16] J. P. Seymour, D. R. Kipke, *Biomaterials* **2007**, *28*, 3594.
- [17] D. H. Szarowski, M. D. Andersen, S. Retterer, A. J. Spence, M. Isaacson, H. G. Craighead, J. N. Turner, W. Shain, *Brain Res.* **2003**, *983*, 23.
- [18] D. J. Edell, V. V. Toi, V. M. McNeil, L. D. Clark, *IEEE Trans. Biomed. Eng.* **1992**, *39*, 635.
- [19] M. A. L. Nicolelis, D. Dimitrov, J. M. Carmena, R. Crist, G. Lehev, J. D. Kralik, S. P. Wise, *Proc. Natl. Acad. Sci. U SA* **2003**, *100*, 11041.
- [20] X. Y. Cui, J. Wiler, M. Dzaman, R. A. Altschuler, D. C. Martin, *Biomaterials* **2003**, *24*, 777.
- [21] L. Kam, W. Shain, J. N. Turner, R. Bizios, *Biomaterials* **2002**, *23*, 511.
- [22] X. Y. Cui, V. A. Lee, Y. Raphael, J. A. Wiler, J. F. Hetke, D. J. Anderson, D. C. Martin, *J. Biomed. Mater. Res.* **2001**, *56*, 261.
- [23] X. Y. Cui, D. C. Martin, *Sens. Actuators, B* **2003**, *89*, 92.
- [24] R. A. Green, N. H. Lovell, G. G. Wallace, L. A. Poole-Warren, *Biomaterials* **2008**, *29*, 3393.
- [25] W. Shain, L. Spataro, J. Dilgen, K. Haverstick, S. Retterer, M. Isaacson, M. Saltzman, J. N. Turner, *IEEE Trans. Neural Syst. Rehab. Eng.* **2003**, *11*, 186.
- [26] L. Spataro, J. Dilgen, S. Retterer, A. J. Spence, M. Isaacson, J. N. Turner, W. Shain, *Exp. Neurol.* **2005**, *194*, 289.
- [27] Z. L. Yue, S. E. Moulton, M. Cook, S. O'Leary, G. G. Wallace, *Adv. Drug Delivery Rev.* **2013**, *65*, 559.
- [28] R. Wadhwa, C. F. Lagenaur, X. T. Cui, *J. Controlled Release* **2006**, *110*, 531.
- [29] R. A. Green, N. H. Lovell, L. A. Poole-Warren, *Acta Biomater.* **2010**, *6*, 63.
- [30] D. D. Ateh, H. A. Navsaria, P. Vadgama, *J. R. Soc., Interface* **2006**, *3*, 741.
- [31] N. K. Guimard, N. Gomez, C. E. Schmidt, *Prog. Polym. Sci.* **2007**, *32*, 876.
- [32] Y. Z. Long, M. M. Li, C. Z. Gu, M. X. Wan, J. L. Duvail, Z. W. Liu, Z. Y. Fan, *Prog. Polym. Sci.* **2011**, *36*, 1415.
- [33] G. Malliaras, M. R. Abidian, *Adv. Mater.* **2015**, *27*, 7492.
- [34] A. J. Heeger, *Angew. Chem. Int. Ed.* **2001**, *40*, 2591.
- [35] R. A. Green, R. T. Hassarati, J. A. Goding, S. Baek, N. H. Lovell, P. J. Martens, L. A. Poole-Warren, *Macromol. Biosci.* **2012**, *12*, 494.
- [36] B. L. Groenendaal, F. Jonas, D. Freitag, H. Pielartzik, J. R. Reynolds, *Adv. Mater.* **2000**, *12*, 481.
- [37] G. Wallace, G. Spinks, *Soft Matter* **2007**, *3*, 665.
- [38] J. Isaksson, P. Kjall, D. Nilsson, N. D. Robinson, M. Berggren, A. Richter-Dahlfors, *Nat. Mater.* **2007**, *6*, 673.
- [39] M. Berggren, A. Richter-Dahlfors, *Adv. Mater.* **2007**, *19*, 3201.
- [40] E. Smela, *Adv. Mater.* **2003**, *15*, 481.
- [41] M. Liu, N. Xu, W. S. Liu, Z. G. Xie, *RSC Adv.* **2016**, *6*, 84269.
- [42] J. Y. Yang, D. C. Martin, *Sens. Actuators, B* **2004**, *101*, 133.
- [43] J. G. Hardy, Z. Z. Khaing, S. J. Xin, L. W. Tien, C. E. Ghezzi, D. J. Mouser, R. C. Sukhvasi, R. C. Preda, E. S. Gil, D. L. Kaplan, C. E. Schmidt, *J. Biomater. Sci., Polym. Ed.* **2015**, *26*, 1327.
- [44] L. T. Qu, G. Q. Shi, J. Y. Yuan, G. Y. Han, F. Chen, *J. Electroanal. Chem.* **2004**, *561*, 149.

- [45] V. Bajpai, P. G. He, L. M. Dai, *Adv. Funct. Mater.* **2004**, *14*, 145.
- [46] J. Y. Lee, C. A. Bashur, A. S. Goldstein, C. E. Schmidt, *Biomaterials* **2009**, *30*, 4325.
- [47] M. R. Abidian, D. C. Martin, *Biomaterials* **2008**, *29*, 1273.
- [48] J. L. Bredas, G. B. Street, *Acc. Chem. Res.* **1985**, *18*, 309.
- [49] A. G. MacDiarmid, *Angew. Chem. Int. Ed.* **2001**, *40*, 2581.
- [50] M. R. Abidian, D. C. Martin, *Adv. Funct. Mater.* **2009**, *19*, 573.
- [51] M. R. Abidian, D. H. Kim, D. C. Martin, *Adv. Mater.* **2006**, *18*, 405.
- [52] G. Yang, K. L. Kampstra, M. R. Abidian, *Adv. Mater.* **2014**, *26*, 4954.
- [53] P. Fattahi, A. Borhan, M. R. Abidian, *Adv. Mater.* **2013**, *25*, 4555.
- [54] S. Takeuchi, P. Garstecki, D. B. Weibel, G. M. Whitesides, *Adv. Mater.* **2005**, *17*, 1067.
- [55] X. L. Luo, X. T. Cui, *Electrochem. Commun.* **2009**, *11*, 402.